Anomalous Nernst effect in the topological and magnetic material $MnBi_4Te_7$

Ceccardi, M.; Zeugner, A.; Folkers, L.C.; Hess, C.; Büchner, B.; Marré, D.; Isaeva, A.; Caglieris, F.

DOI
10.1038/s41535-023-00606-2

Publication date
2023

Document Version
Final published version

Published in
npj Quantum Materials

npj | quantum materials

www.nature.com/npjquantmats

ARTICLE OPEN

Anomalous Nernst effect in the topological and magnetic material $MnBi_4Te_7$

M. Ceccardi[1,2✉], A. Zeugner[3], L. C. Folkers[4,5], C. Hess[4,6,7], B. Büchner[4,5,7], D. Marré[1,2], A. Isaeva[4,8] and F. Caglieris[1,2,4✉]

The recently discovered magnetic topological insulators $(MnBi_2Te_4)(Bi_2Te_3)_n$, $n = 0$–4, are an ideal playground to study the influence of magnetic properties on band topology, giving access to diverse quantum states in a single compound. In the low temperature-antiferromagnetic state and vanishing magnetic field, the $n = 1$ system is a topological insulator protected by a combination of time reversal and a translation symmetries. It has been argued that, when the antiferromagnetic phase is forced to a the fully spin polarized state by the application of an external magnetic field, this system develops Weyl cones in the conduction band, which become accessible in presence of an intrinsic electronic doping. In this work, we experimentally prove the raising of field-induced Weyl state through the detection of an intrinsic anomalous Nernst effect in a bulk single crystal of $MnBi_4Te_7$.

npj Quantum Materials (2023)8:76 ; https://doi.org/10.1038/s41535-023-00606-2

INTRODUCTION

Magnetic topological materials, such as magnetic topological insulators (MTI)[1–5] and magnetic Weyl semimetals (MWS)[6–8], are intriguing playgrounds, in which a magnetic order is combined with a topological band structure. A proper control of the magnetic ground state in these systems can strongly influence their topological properties[9–12], giving access to diverse quantum states in a single material system. For instance, the idea that a Weyl semimetal (WS) state could be realized in a 3D Topological Insulator (TI) was firstly envisioned a decade ago[6,9]: considering an effective model of a bulk multi-layer structure composed of identical thin films of a magnetically doped 3D TI separated by ordinary-insulator spacer layers, it was proposed that a ferromagnetic (FM) order can create a WS phase by properly tuning some parameters like the hopping between planes and the exchange coupling[6,9].

Recently discovered intrinsic MTI $(MnBi_2Te_4)(Bi_2Te_3)_n$, $n = 0$–4, (MBTn) have been pointed out as an ideal platform to experimentally realize the transition between different topological states[2,4,5,13–23]. In these materials, a quintuple layered (QL) fragment Te-Bi-Te-Bi-Te of prototypical 3D TI Bi_2Te_3 is interlaced by Mn-Te bi-layers: the resulting septuple layers (SLs) are held together by Van der Waals forces, and their stackings generate new Van der Waals materials, which preserve the TI nature but host at the same time a tunable magnetic ground state originated by the Mn^{2+} ions.

The $n = 0$ progenitor of the family $MnBi_2Te_4$ (Mn124)[4,13–15,24,25] is characterized by an out-of-plane FM coupling in the Mnplanes and by an interlayer antiferromagnetic (AFM) coupling, which produces an A-type AFM ordering below a Néel temperature $T_N = 25$ K[4]. The band structure of a bulk crystal is insulating, having the conduction and the valence band divided by a small gap[4]. Below the antiferromagnetic transition, there is a Dirac surface state in the gap protected by a combination of the time-reversal and a translation symmetries[4]. Furthermore, following the effective model of a bulk multi-layer structure composed of identical thin films of a magnetically doped 3D TI separated by ordinary-insulator spacer layer[9], Mn124 has been modeled in the FM regime— obtainable when all the spins are aligned applying an external out-of-plane magnetic field of some Tesla in the AFM phase— revealing the presence of Weyl nodes in the gap[10]. In addition, this result was confirmed also performing DFT+U calculations[26]. To sum up, a topological phase transition can emerge driving the Mn124 AFM system to a fully spin-polarized state by a sufficiently high external out-of-plane magnetic field.

Moving across the series, the insertion of *n*-QL between the SLs enhances the distance between the magnetic atomic planes and, inevitably, weakens the interlayer AFM interaction[19,20]. This happens in the $MnBi_4Te_7$ (Mn147) compound[5,17], in which it has been estimated that the total energy associated with the configuration with an AFM order among Mnatomic planes is comparable to the energy of the FM order[5,17,27] and the energy difference between the FM and AFM configurations is 0.5 meV/Mn[5]. This condition pushes the system into a complex scenario, in which different magnetic states compete. The result is a decrease of the AFM Néel temperature down to $T_N = 12.5$ K in Mn147, with a FM-like rearrangement below *T* around 6 K[5,17]. Applying the effective model to Mn147 the result is different from its ancestor[10], despite the fact that the bulk bands are similar[5,17]. It has been calculated that, in the FM regime, the bulk gap should be only reduced to 30 meV, without closing in the Weyl nodes. The key concept is that the hopping between the magnetic planes is too weak[10]. Although DFT+U calculations substantially confirmed this result[5], they also revealed that a ferromagnetic component can split the double degeneracy of the bulk bands, creating Weyl nodes only 24 meV and 70 meV above the gap, very close to the bottom of the conduction band[5]. Hence, Weyl physics is expected to emerge when the Mn147 AFM system is driven to a fully spin-polarized state by a sufficiently high external magnetic field. Weyl nodes in the band structure are sources or sinks of Berry curvature, the gauge field associated to the geometrical phase of the electrons. A finite Berry curvature is responsible for anomalous electric and thermoelectric transport properties[6,28], including the

[1]University of Genova, Department of Physics, Via Dodecaneso 33, 16146 Genova, Italy. [2]CNR-SPIN Institute, Corso Perrone 24, 16142 Genova, Italy. [3]Institute for Inorganic Chemistry II, TU Dresden, 01069 Dresden, Germany. [4]Leibniz Institute for Solid State and Materials Research, 01069 Dresden, Germany. [5]Institut für Festkörperphysik, TU Dresden, 01069 Dresden, Germany. [6]Fakultät für Mathematik und Naturwissenschaften, Bergische Universität Wuppertal, 42119 Wuppertal, Germany. [7]Center for Transport and Devices, TU Dresden, 01069 Dresden, Germany. [8]Institute of Physics, University of Amsterdam, 1098 XH Amsterdam, The Netherlands. ✉email: michele.ceccardi@edu.unige.it; federico.caglieris@spin.cnr.it

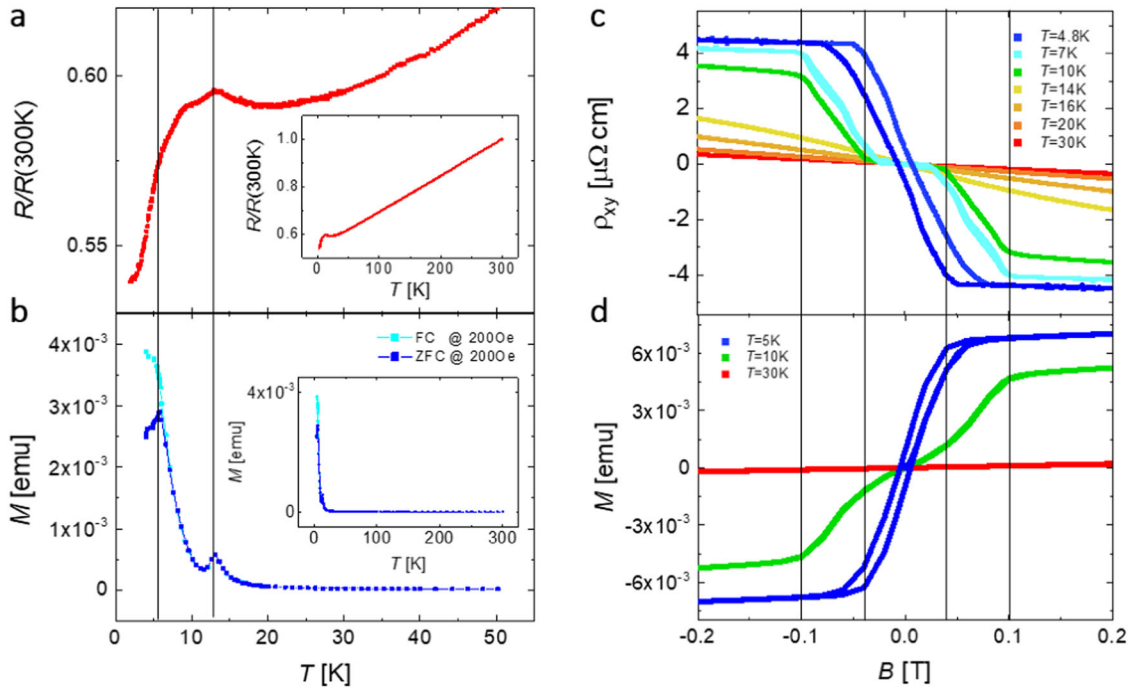

Fig. 1 Magnetic and transport properties of a $MnBi_4Te_7$ single crystal. a Temperature dependence of resistance normalized to the 300 K value in the transition region. Inset, overview from room to low temperature. **b** Magnetization as a function of temperature measured in an out-of-plane magnetic field in ZFC and FC conditions. Inset, overview from room to low temperature. Vertical black lines in panels (**a**), (**b**) are drawn at the correspondence of the antiferromagnetic transition or the ferromagnetic-like one at $T = 12.4$ K and $T \approx 5$ K. **c** Magnetic field dependence of the Hall resistivity measured for 4.8 K < T < 30 K. **d** The Magnetization as a function of the out-of-plane magnetic field for $T = 5$ K, 10 K, 30 K applied in the out-of-plane direction. Vertical black lines in panels (**c**), (**d**) are drawn at the correspondence of the spin flop transition ($B \approx 0.04$ T) at $T = 10$ K and the saturation field ($B \approx 0.1$ T) at $T = 5$ K.

anomalous Nernst effect (ANE)[29–34]. The Nernst effect is the thermoelectric counterpart of the Hall effect, being a transverse voltage in response to a longitudinal thermal gradient. Normally, to generate a finite Nernst signal in a conducting material, the charge carriers, that flow along the thermal gradient, must be crosswise deflected by the application of an external out-of-plane magnetic field B. The induced transverse voltage is then directly proportional to B. A departure from this trend is often identified as ANE, whose fingerprint is a finite Nernst signal for vanishing magnetic fields, which remains almost constant with an increasing B. This behavior was traditionally observed in several ferromagnets, where the ANE was phenomenological related to their large magnetization. The physical origin of the ANE has been then identified either with an extrinsic or an intrinsic mechanism. The former corresponds to the side-jump scattering or the skew scattering by impurities[35], while the latter has been described through of the Berry phase formalism[35,36]. The introduction of the Berry curvature concept not only provided an intrinsic microscopic mechanism for the ANE, depending only on the band structure, but also allowed the prediction of anomalous transport properties beyond ferromagnetic materials, recently confirmed by the experimental observation of a large ANE in non-collinear antiferromagnets and in non-magnetic Weyl semimetals[7,31–33]. Hence, to generate an intrinsic ANE, it is necessary to have hotspots of Berry curvature and the Weyl nodes are a perfect practical realization[29–33]. This intimate link between the ANE and the Weyl points makes the Nernst effect itself a powerful probe to classify a material as a Weyl semimetal.

In this paper, we investigate the Nernst effect of a bulk crystal of Mn147 in the temperature range 7 K < T < 30 K across the antiferromagnetic transition. We show that a sizable ANE appears at sufficiently high out-of-plane magnetic fields for 7 K < T < 20 K and, since this is, as state above, a clear evidence for finite Berry curvature at the Fermi level, we associate it to the presence of the cited Weyl points in the conduction band, when the fully spin-polarized state is established.

RESULTS

Magnetic and transport properties

Figure 1a displays the T-dependence of the electrical resistivity (normalized to the room-temperature value) ρ/ρ(300K) of the Mn147 sample. The resistivity at 10 K is $\rho \approx 0.15$ mΩ cm, consistent with other works in literature[5,17,19]. The T-dependence shows a metallic behavior, with ρ/ρ(300 K) decreasing almost linearly down to $T \approx 30$ K[5,17] (inset of Fig. 1a). For $T < 30$ K the resistivity undergoes an upturn, attributed to the enhancement of magnetic fluctuations[17] when the system approaches the antiferromagnetic transition. At $T_N = 12.4$ K a steep decrease of ρ occurs. The broadening of the transition is related to the strong intraplane ferromagnetic correlations, which persist up to about 30 K, as also confirmed through high-frequency ESR[5]. In addition, a second anomaly at $T \approx 5$ K is caused by the FM-like rearrangement of the magnetic structure[5,19]. The evolution of the magnetic ground state emerges also in the temperature dependence of the magnetization (M) curves (Fig. 1b) measured in an out-of-plane magnetic field of 0.02 T: on the one hand, at the AFM transition, there is a sudden decrease of the magnetization; on the other, at the FM-like rearrangement, there is a splitting between the curves obtained in zero-field-cooling (ZFC) and field-cooling (FC) conditions, with an overall increase of M[5].

The field dependence of the isothermal Hall resistivity ρ_{xy} is displayed in Fig. 1c and it mimics the behavior of the magnetization as a function of the external out-of-plane magnetic field reported as a comparison in Fig. 1d. The overall negative slopes of the Hall curves indicate electron-type bulk charge carriers and, from the linear regime at $T = 30$ K, we can extract the

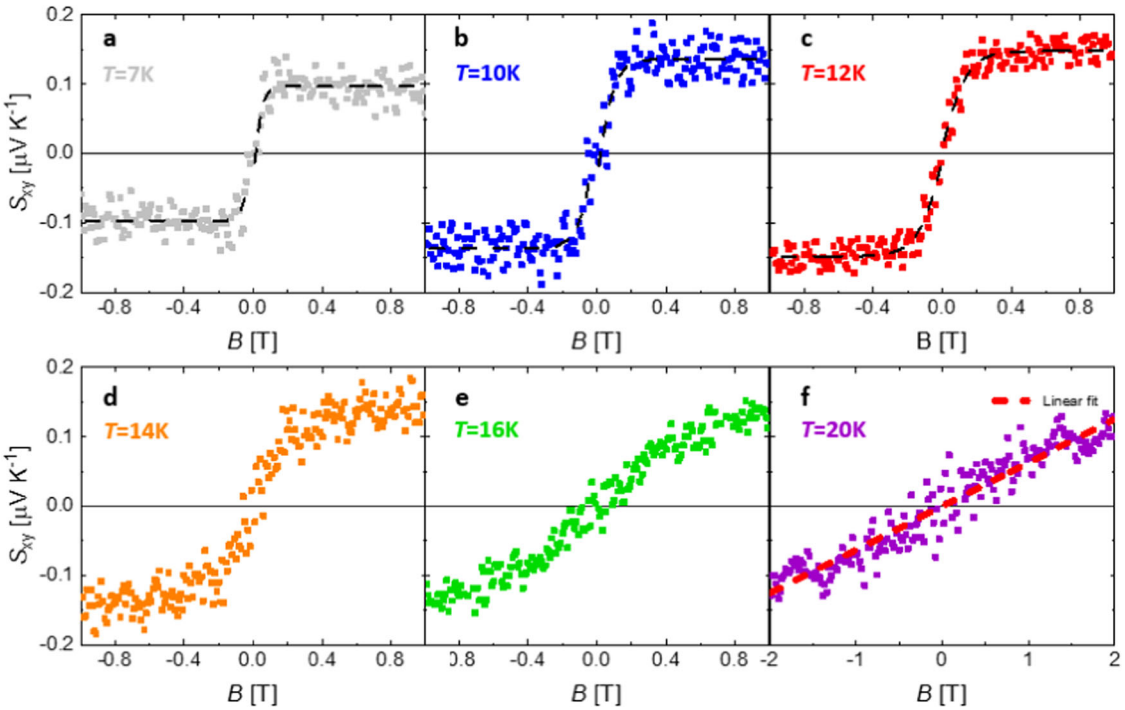

Fig. 2 The Nernst coefficient of a $MnBi_4Te_7$ single crystal. a–e The Nernst effect as a function of temperature and out-of-plane magnetic field for 7 K < T < 16 K and −1 T < B < 1 T; the black lines are guides for the eyes. **f** The Nernst coefficient at T = 20 K, considering −2 T < B < 2 T and linear fit.

electron density to be 3×10^{20} cm^{-3}. Moreover, below the Nèel temperature, we report the anomalous Hall effect (AHE), measuring the saturation for the fields greater than ≈ 0.1 T, when the fully spin-polarized state is reached, as can be established by the plateaux of the magnetization curves in Fig. 1d. In the Supplementary Figure 3 we provided details on how the anomalous Hall contribution (ρ^A_{xy}) can be evaluated from the total Hall effect (ρ_{xy}). The saturation value of ρ^A_{xy} ranges from $\rho^A_{xy} \approx 3.5$ μΩ cm to $\rho^A_{xy} \approx 4.5$ μΩ cm. At 10 K the anomalous Hall conductivity is $\sigma^A_{xy} \approx \rho^A_{xy}/\rho^2_{xx} = 144\,\Omega^{-1}$ cm^{-1}, of the same order of magnitude compared to the previous literature[17,27]. In addition, the Hall resistivity faithfully mimics the behavior of the magnetization as a function of the applied field also at low fields, showing a metamagnetic spin-flop feature in the AFM regime (T = 7 K, 10 K) as well as a hysteretic behavior linked to the FM-like rearrangement (T = 4.8 K)[5,17]. The vertical black lines in panels c, d, in correspondence of the spin flop transition ($B \approx 0.04$ T) at T = 10 K and the saturation field ($B \approx 0.1$ T) at T = 5 K, are drawn to underline the comparison between the Hall resistivity and magnetization curves.

The anomalous Nernst effect

A photo of the experimental set-up for thermoelectric transport properties is reported in the supplementary Figure 1. Figure 2 exhibits the evolution of the B-dependence of the antisymmetrized Nernst coefficient S_{xy} at different temperatures (see Supplementary Figure 2 for details about the antisymmetrization process). For 7 K < T < 12 K, in the AFM phase, the compound develops an evident step-like ANE (Fig. 2a–c). As it can be inferred from Fig. 2, below the antiferromagnetic transition, the Nernst signal is dominated by the anomalous Nernst component (S^A_{xy}) and the amplitude of S^A_{xy} results to range from $S^A_{xy} \approx 0.1$ μV K^{-1} to $S^A_{xy} \approx 0.15$ μV K^{-1}. As a phenomenological approach[37], we assumed that $S^A_{xy} = A \tanh \frac{B}{B_s}$, where A is the saturating value and B_s is the saturating field. The fitted curves are superimposed to the data as a guide for the eyes. At T = 7 K, $B_s \approx 0.05$ T, is relatively small compared to standard ferromagnetic materials and it increases warming up. Interestingly, the anomalous Nernst coefficient persists at 14 K (Fig. 2d), slightly above the magnetic transition temperature in the resistivity, and it almost disappears at 16 K—at least for B < 1 T—(Fig. 2e). In the Supplementary Figure 3 we explained how S^A_{xy} was evaluated above the antiferromagnetic transition.

In the paramagnetic regime at T = 20 K, S_{xy} is very small and it shows the usual linear trend in B (Fig. 2f): the absolute value of the standard Nernst coefficient at 20 K is $\nu = S_{xy}/B = 63 \pm 2$ nV K^{-1} T^{-1}, obtained by the linear fit of the data. In a single band model within a Fermi liquid scenario, the magnitude of ν is linked to the other transport properties by the relation: $\nu B \approx S_{xx} \tan\theta_H$[38,39], where S_{xx} is the Seebeck coefficient and $\tan\theta_H = \sigma_{xy}/\sigma_{xx}$ the tangent of the Hall angle. In our sample, at T = 20 K, $\tan\theta_H/B = (0.068 \pm 0.002)$ T^{-1} and $S_{xx} \approx -1$ μV K^{-1} (see Supplementary Figure 5), in good agreement with the ν value.

DISCUSSION

The metallic-like behavior of the resistivity as a function of the temperature (Fig. 1a) suggests that the Fermi level of our Mn147 bulk single crystal is positioned in the conduction band. In addition, the negative linear slope of the Hall coefficient at T = 16 K and T = 20 K (in the paramagnetic state) as a function of the magnetic field (Fig. 1c) confirms the electronic-like type of the dominant charge carriers. This is in agreement with previous reports, where a certain degree of electronic doping is attributed to Mn-Bi intermixing and Mnvacancies[5,22]. Furthermore, the ARPES measurements in ref. [5], performed on single crystals of the same batch as we use in this work, show the Fermi level positioned about 100 meV above the bottom of the conduction band. Hence, it is natural that the transport properties of our sample are dominated by the conduction band electrons, rather than by the topologically protected surface states. On the one hand, this condition prevents the exploitation of the material as a 3D AFM TI.

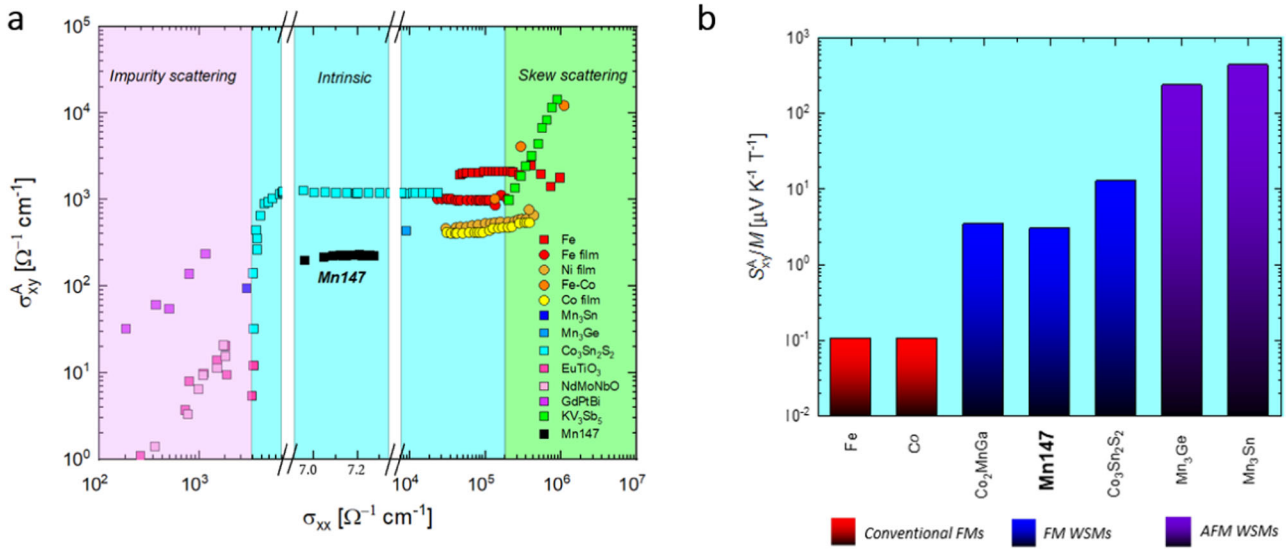

Fig. 3 Topological nature of the anomalous contributions. a Overview of the Anomalous Hall Effect: the anomalous transverse conductivity (σ_{xy}^{A}) versus longitudinal electric conductivity (σ_{xx}) for some materials, spanning the extrinsic and intrinsic mechanisms. The $MnBi_4Te_7$ fall in the intrinsic region. Adapted from refs. [29,40]. **b** Anomalous Nernst effect normalized to the magnetization value for various kinds of magnets. The conventional ferromagnets are depicted in red; the ferromagnetic Weyls Semimetals (FM WSMs) in blue and the antiferromagnetic Weyls Semimetals (AFM WSMs) in purple. S_{xy}/M for $MnBi_4Te_7$ is comparable to FM WSMs. Adapted from ref. [31].

On the other hand, the observed ANE—if intrinsic—is the fingerprint for the presence of hotspots of Berry curvature close to the Fermi level. In fact, the intrinsic ANE is only determined by the Berry curvature in proximity of the Fermi level, since the entropy density is non-zero only for partially unoccupied bands. This substantially differs the ANE from the AHE, which is obtained by an integration of the Berry curvature over all the occupied bands[36].

The intrinsic nature of anomalous transport in Mn147 can be verified by relating the AHE conductivity (σ_{xy}^{A}) to the longitudinal conductivity σ_{xx}[29,35,40,41]. More specifically, three different regimes can be found, as shown in Fig. 3a in a map of the AHE for different materials. Firstly, in case of a dominant intrinsic effect, σ_{xy}^{A} displays a plateau-like behavior as a function of σ_{xx} ($\sigma_{xy}^{A} \approx const$), considering that the anomalous response does not depend directly on the scattering time[35]. This is typically realized in the middle range $10^3\ \Omega^{-1}\ cm^{-1} < \sigma_{xx} < 10^6\ \Omega^{-1}\ cm^{-1}$ [35]. It is worth to mention that the side-jump scattering mechanism, which can be found in low conductivity systems ($\sigma_{xx} < 10^3$), yields to an identical scaling relation to that of intrinsic AHE ($\sigma_{xy}^{A} \approx const$), though its magnitude is predicted to be much smaller than the intrinsic one[35]. On the contrary, the contribution of the skew scattering is commonly reported in the high-conductivity regime ($\sigma_{xx} > 10^6\ \Omega^{-1}\ cm^{-1}$), with a linear relation $\sigma_{xy}^{A} \propto \sigma_{xx}$[29,35,40]. In our case, as is depicted in the AHE map, both the value of $\sigma_{xx} \approx 10^4\ \Omega^{-1}\ cm^{-1}$ and the constant behavior of σ_{xy}^{A} are the fingerprint of an intrinsic phenomenon. This confirms the non-vanishing Berry curvature at the Fermi level as the main candidate to explain the measured ANE in Mn147.

The presence of the Berry curvature at the Fermi level is not necessary linked to a topological protection[35]; indeed, also conventional ferromagnets display an intrinsic ANE due to a finite Berry curvature at the Fermi level originated by the huge net magnetization[31,35]. The amplitude of the ANE in Mn147 is comparable to standard ferromagnets, but the net magnetization (M) is moderate. In the fully polarized state at 10 K, M ≈ 53 mT, considering the magnetic measurements performed on single crystals of the same batch[5], and it is more than one order of magnitude smaller compared to standard ferromagnets[31,42]. Moreover, Fig. 3b displays the anomalous Nernst effect normalized to M for some selected magnets. Considering conventional ferromagnets (red) the ANE is proportional to the magnetization and the ratio between these two quantities does not exceed 1 $\mu V\ K^{-1}\ T^{-1}$. For topological magnets (blue and purple), instead, the ANE is much more enhanced than the empirical linear relation[31]. In particular, S_{xy}/M for Mn147 is comparable to other ferromagnetic Weyl Semimetals (blue), such as $Co_3Sn_2S_2$[29] and Co_2MnGa[34]. In addition, the anomalous Nernst conductivity $\alpha_{xy} = (0.9 \pm 0.1)\ A\ K^{-1}\ m^{-1}$ at low temperature, compatible to other ferromagnetic Weyl semimetals[29] (see the Supplementary Figure 4 for the details).

For these reasons, the Weyl cones, predicted by DFT+U calculations[5], are the main candidates to explain the observed ANE. Based on the Nernst measurements in Fig. 2, we traced a topological phase diagram of Mn147 (Fig. 4), where the magnetic field-derivative of the Nernst effect is presented in a color map as a function of temperature and out-of-plane magnetic field. At small magnetic field and below the Neél temperature the system is an AFM TI, although one needs to shift the Fermi level into the bulk gap to access the protected surface states. In our case, with *E*F in conduction band, the material behaves as a standard metal. By increasing the magnetic field, a fully spin polarized magnetic state is obtained. This forced ferromagnetism splits the double degeneracy of the bulk bands and two pairs of Weyl nodes in the conduction band appear[5]. This corresponds to a saturation of S_{xy}, with dS_{xy}/dB tending to zero. This regime is represented by the orange region in the phase diagram where the system is identified as a ferromagnetic Weyl semimetal (FM WS). The brown dots superimposed to the diagram are obtained from the effective saturation of the curves in Fig. 2 ($B > 3B_s$); the black and the green dashed lines are based on the magnetic measurements on single crystals of the same batch[5].

Finally, we reported that the anomalous Nernst effect is still present slightly above the antiferromagnetic transition (the AHE shows the same behavior as is reported in the Supplementary Figure 3) and this suggests that the fully polarized state can be reached also at $T > 12.4$ K. The fact can be confirmed by the temperature dependence of the magnetization curve at $B = 200$ mT, reported in[5] and performed on a crsystal of the same batch: the onset of the ferromagnetic transition is above the

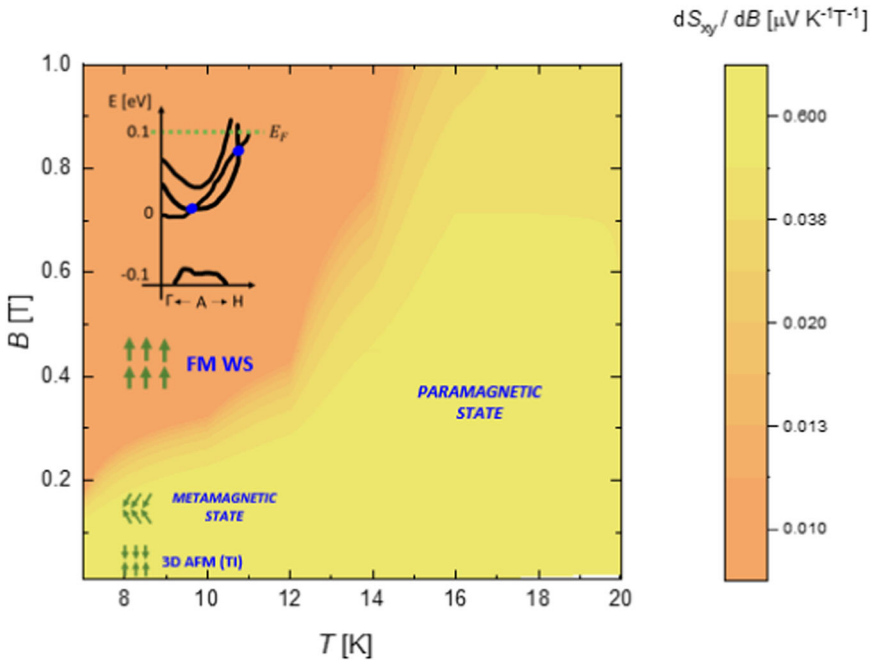

Fig. 4 Topological phase diagram of $MnBi_4Te_7$ as a function of temperature and out-of-plane magnetic field across the antiferromagnetic transition. The colored map is based on Nernst measurements in Fig. 2 and the black/green dashed lines indicate the magnetic transitions reported in magnetic measurements in ref. [5]. The AFM phase for vanishing magnetic fields is linked to a 3D TI state, although one needs to shift the Fermi level into the bulk gap to access the protected surface states. The fully spin-polarized phase is linked to the Weyl cones, detected by the ANE. As an inset, there is a sketch of the bulk bands adapted from ref. [5] (see text for details).

antiferromagnetic one (detected at $B = 20$ mT). The fully polarized state is stabilized both by the presence of the external magnetic field and by the ferromagnetic correlations up to about 30 K[5].

In conclusion, we detected an intrinsic ANE in a bulk single crystal of $MnBi_4Te_7$ across its antiferromagnetic transition, by driving the system into a fully spin-polarized state through the application of an external out-of-plane magnetic field. The breaking of the time-reversal symmetry yields to the two pairs of the Weyl nodes, responsible for the intrinsic ANE, in the conduction band[5,36], where the Fermi level is positioned thanks to a natural doping of the compound[5]. The series MBTn appears to be a flexible playground to understand, probe and control phenomena related to non-trivial topology, ranging from the Weyl Fermiology[5,10,26] to the quantum anomalous Hall effect[13] and the axion physics[14,15]. The possibility of switching across different quantum states by tuning knobs such as magnetic field, electric field, temperature, strain and dimensionality, traces the route towards novel devices and the investigation of systems hosting multiple topological states is a fundamental base[10–12,15,43,44].

METHODS

Crystal growth

Single crystals of Mn147 were grown following the procedures in ref. [5]. Samples were characterized by energy-dispersive X-ray spectroscopy (EDX) on a Hitachi SU8020 microscope equipped with a X-MaxN (Oxford) Silicon Drift Detector (SDD) with 20 kV acceleration voltage and 100 s accumulation time. The results confirmed Mnsub-stoichiometry in our samples according to an average formula $Mn_{0.8}Bi_{4.3}Te_7$. Crystal structure of a selected crystal was analyzed by single-crystal X-ray diffraction, the details are presented in ref. [5]. Several crystals used in this study were extracted from the same batch as the ones in ref. [5] and ref. [22].

Transport measurement on bulk crystals

The measured crystal has a size of about $0.8 \times 0.5 \times 0.1$ mm^3. For the resistivity and Hall effect measurements, we applied a standard four-probe method with 50-μm-thick copper wires glued on the sample via copper wires as electrodes. For the Nernst effect characterization, the sample has been glued along the *ab*-plane on a $SrTiO_3$ insulating substrate used as a support due to the limited size of the sample. The heating power has been applied using a 2.7 kΩ resistive heater connected on the one side of the sample with a thermal glue (Stycast 2500ft with catalyst 9), while a cold finger on the other side of the sample, made with a silver wire, has been connected to the thermal mass in order to complete the thermal circuit. The thermal gradient across the sample has been measured using a chromel-Au-chromel thermocouple, calibrated as a function of the temperature T and the out-of-plane magnetic field B. The transport measurements were performed in an Oxford cryostat endowed with a 15/17T magnet and in a Quantum Design Physical Property Measurement System (PPMS) with a 9T-magnet.

Magnetic measurements

The out-of-plane magnetic measurements as a function of temperature and magnetic field were performed using a SQUID (MPMS Quantum Design). The temperature-dependent magnetization measurements were acquired in external magnetic fields of 0.02T for both zero-field-cooled (ZFC) and field-cooled-warming (FC) conditions.

DATA AVAILABILITY

The numerical data shown in the figures of this manuscript can be downloaded from the Zenodo online repository: https://zenodo.org/records/10083599.

Received: 9 June 2023; Accepted: 23 November 2023;
Published online: 18 December 2023

REFERENCES

1. Tokura, Y., Yasuda, K. & Tsukazaki, A. Magnetic topological insulators. *Nat. Rev. Phys.* **1**, 126–143 (2019).
2. Fei, F. et al. The material efforts for quantized Hall devices based on topological insulators. *Adv. Mater.* **32**, 1904593 (2020).
3. Weng, H., Yu, R., Hu, X., Dai, X. & Fang, Z. Quantum anomalous Hall effect and related topological electronic states. *Adv. Phys.* **64**, 227–282 (2015).
4. Otrokov, M. M. et al. Prediction and observation of an antiferromagnetic topological insulator. *Nature* **576**, 416–422 (2019).
5. Vidal, R. C. et al. Topological electronic structure and intrinsic magnetization in $MnBi_4Te_7$: a Bi_2Te_3 derivative with a periodic Mn sublattice. *Phys. Rev. X* **9**, 041065 (2019).
6. Armitage, N., Mele, E. & Vishwanath, A. Weyl and Dirac semimetals in three-dimensional solids. *Rev. Mod. Phys.* **90**, 015001 (2018).
7. Nayak, A. K. et al. Large anomalous Hall effect driven by a nonvanishing Berry curvature in the noncolinear antiferromagnet Mn_3Ge. *Sci. Adv.* **2**, e1501870 (2016).
8. Wang, Q. et al. Large intrinsic anomalous Hall effect in half-metallic ferromagnet $Co_3Sn_2S_2$ with magnetic Weyl Fermions. *Nat. Commun.* **9**, 1–8 (2018).
9. Burkov, A. & Balents, L. Weyl semimetal in a topological insulator multilayer. *Phys. Rev. Lett.* **107**, 127205 (2011).
10. Lei, C., Chen, S. & MacDonald, A. H. Magnetized topological insulator multilayers. *PNAS* **117**, 27224–27230 (2020).
11. Soh, J.-R. et al. Ideal Weyl semimetal induced by magnetic exchange. *Phys. Rev. B* **100**, 201102 (2019).
12. Ikhlas, M. et al. Piezomagnetic switching of the anomalous Hall effect in an antiferromagnet at room temperature. *Nat. Phys.* **18**, 1086–1093 (2022).
13. Deng, Y. et al. Quantum anomalous Hall effect in intrinsic magnetic topological insulator $MnBi_2Te_4$. *Science* **367**, 895–900 (2020).
14. Liu, C. et al. Robust axion insulator and Chern insulator phases in a two-dimensional antiferromagnetic topological insulator. *Nat. Mater.* **19**, 522–527 (2020).
15. Gao, A. et al. Layer Hall effect in a 2D topological axion antiferromagnet. *Nature* **595**, 521–525 (2021).
16. Ge, J. et al. High-chern-number and high-temperature quantum Hall effect without Landau levels. *Natl Sci. Rev.* **7**, 1280–1287 (2020).
17. Hu, C. et al. A Van der Waals antiferromagnetic topological insulator with weak interlayer magnetic coupling. *Nat. Commun.* **11**, 1–8 (2020).
18. Hu, C. et al. Realization of an intrinsic ferromagnetic topological state in $MnBi_8Te1_3$. *Sci. Adv.* **6**, eaba4275 (2020).
19. Klimovskikh, I. I. et al. Tunable 3D/2D magnetism in the $(MnBi_2Te_4)(Bi_2Te_3)$ m topological insulators family. *npj Quantum Mater.* **5**, 54 (2020).
20. Wu, J. et al. Toward 2D magnets in the $(MnBi_2Te_4)(Bi_2Te_3)$ n bulk crystal. *Adv. Mater.* **32**, 2001815 (2020).
21. He, K. MnBi2Te4-family intrinsic magnetic topological materials. *npj Quantum Mater.* **5**, 90 (2020).
22. Vidal, R. et al. Orbital complexity in intrinsic magnetic topological insulators $MnBi_4Te_7$ and $MnBi_6Te_{10}$. *Phys. Rev. Lett.* **126**, 176403 (2021).
23. Wang, H. et al. Possible bipolar effect inducing anomalous transport behavior in the magnetic topological insulator $Mn(Bi_{1-x}Sb_x)_2Te_4$. *Phys. Rev. B* **103**, 085126 (2021).
24. Bac, S.-K. et al. Topological response of the anomalous Hall effect in $MnBi_2Te_4$ due to magnetic canting. *npj Quantum Mater.* **7**, 46 (2022).
25. Garnica, M. et al. Native point defects and their implications for the Dirac point gap at $MnBi_2Te_4$ (0001). *npj Quantum Mater.* **7**, 7 (2022).
26. Li, J. et al. Intrinsic magnetic topological insulators in Van der Waals layered $MnBi_2Te_4$-family materials. *Sci. Adv.* **5**, eaaw5685 (2019).
27. Wu, J. et al. Natural Van der Waals heterostructural single crystals with both magnetic and topological properties. *Sci. Adv.* **5**, eaax9989 (2019).
28. Mercaldo, M. T., Noce, C., Caviglia, A. D., Cuoco, M. & Ortix, C. Orbital design of Berry curvature: pinch points and giant dipoles induced by crystal fields. *npj Quantum Mater.* **8**, 12 (2023).
29. Yang, H. et al. Giant anomalous Nernst effect in the magnetic Weyl semimetal $Co_3Sn_2S_2$. *Phys. Rev. Mater.* **4**, 024202 (2020).
30. Sakai, A. et al. Giant anomalous Nernst effect and quantum-critical scaling in a ferromagnetic semimetal. *Nat. Phys.* **14**, 1119–1124 (2018).
31. Ikhlas, M. et al. Large anomalous Nernst effect at room temperature in a chiral antiferromagnet. *Nat. Phys.* **13**, 1085–1090 (2017).
32. Caglieris, F. et al. Anomalous Nernst effect and field-induced Lifshitz transition in the Weyl semimetals TaP and TaAs. *Phys. Rev. B* **98**, 201107 (2018).
33. Wuttke, C. et al. Berry curvature unravelled by the anomalous Nernst effect in Mn_3Ge. *Phys. Rev. B* **100**, 085111 (2019).
34. Guin, S. N. et al. Anomalous Nernst effect beyond the magnetization scaling relation in the ferromagnetic Heusler compound Co_2MnGa. *NPG Asia Mater.* **11**, 16 (2019).
35. Nagaosa, N., Sinova, J., Onoda, S., MacDonald, A. H. & Ong, N. P. Anomalous Hall effect. *Rev. Mod. Phys.* **82**, 1539 (2010).
36. Xiao, D., Chang, M.-C. & Niu, Q. Berry phase effects on electronic properties. *Rev. Mod. Phys.* **82**, 1959 (2010).
37. Liang, T. et al. Anomalous Nernst effect in the Dirac semimetal Cd_3As_2. *Phys. Rev. Lett.* **118**, 136601 (2017).
38. Behnia, K. The Nernst effect and the boundaries of the Fermi liquid picture. *J. Condens. Matter Phys.* **21**, 113101 (2009).
39. Pallecchi, I., Caglieris, F. & Putti, M. Thermoelectric properties of iron-based superconductors and parent compounds. *Supercond. Sci. Technol.,* **29**, 073002 (2016).
40. Fujishiro, Y. et al. Giant anomalous Hall effect from spin-chirality scattering in a chiral magnet. *Nat. Commun.* **12**, 1–6 (2021).
41. Onoda, S., Sugimoto, N. & Nagaosa, N. Quantum transport theory of anomalous electric, thermoelectric, and thermal Hall effects in ferromagnets. *Phys. Rev. B* **77**, 165103 (2008).
42. Perdew, J. P., Burke, K. & Ernzerhof, M. Generalized gradient approximation made simple. *Phys. Rev. Lett.* **77**, 3865 (1996).
43. Sakai, A. et al. Iron-based binary ferromagnets for transverse thermoelectric conversion. *Nature* **581**, 53–57 (2020).
44. Fan, Y. et al. Magnetization switching through giant spin–orbit torque in a magnetically doped topological insulator heterostructure. *Nat. Mater.* **13**, 699–704 (2014).

ACKNOWLEDGEMENTS

This project has been supported by the Deutsche Forschungsgemeinschaft (DFG) through the Collaborative Research Center 1143 (project ID 247310070) and the Würzburg-Dresden Cluster of Excellence ct.qmat (EXC 2147, project ID 390858490). F.C. acknowledges the European Union's Horizon 2020 research and innovation program under the Marie Skiodowska-Curie. grant agreement No. 8927728. M.C. and D.M. acknowledge the financial support from the Università di Genova through the "Fondi di Ricerca di Ateneo" (FRA).

AUTHOR CONTRIBUTIONS

F.C., B.B., C.H., and D.M. planned and coordinated the project. M.C. and F.C. performed the transport measurements and the data analysis. A.I., A.Z., and L.C.F. synthetized the samples. M.C., F.C., and D.M. wrote the paper with inputs from all authors.

COMPETING INTERESTS

The authors declare no competing interests.

ADDITIONAL INFORMATION

Supplementary information The online version contains supplementary material available at https://doi.org/10.1038/s41535-023-00606-2.

Correspondence and requests for materials should be addressed to M. Ceccardi or F. Caglieris.

Reprints and permission information is available at http://www.nature.com/reprints

Publisher's note Springer Nature remains neutral with regard to jurisdictional claims in published maps and institutional affiliations.